Preprints (www.preprints.org) | NOT PEER-REVIEWED | Posted: 25 January 2018 doi:10.20944/preprints201801.0235.v1

Article

Utilizing UAV and 3D Computer Vision for Visual Inspection of a Large Gravity Dam

Ali Khaloo [1], David Lattanzi [1,*] and Adam Jachimowicz [2]

[1] Department of Civil, Environmental, and Infrastructure Engineering, George Mason University, Fairfax, VA, USA, 22030; akhaloo@gmu.edu (A.K.); dlattanz@gmu.edu (D.L.)
[2] Argonne National Laboratory, Washington, D.C., USA, 20024; ajachimowicz@anl.gov
* Correspondence: dlattanz@gmu.edu; Tel.: +1-703-993-3695

Abstract: Dams are a critical infrastructure system for many communities, but they are also one of the most challenging to inspect. Dams are typically very large and complex structures, and the result is that inspections are often time-intensive and require expensive, specialized equipment and training to provide inspectors with comprehensive access to the structure. The scale and nature of dam inspections also introduces additional safety risks to the inspectors. Unmanned aerial vehicles (UAV) have the potential to address many of these challenges, particularly when used as a data acquisition platform for photogrammetric three-dimensional (3D) reconstruction and analysis, though the nature of both UAV and modern photogrammetric methods necessitates careful planning and coordination for integration. This paper presents a case study on one such integration at the Brighton Dam, a large-scale concrete gravity dam in Maryland, USA. A combination of multiple UAV platforms and multi-scale photogrammetry was used to create two comprehensive and high-resolution 3D point clouds of the dam and surrounding environment at intervals. These models were then assessed for their overall quality, as well as their ability to resolve flaws and defects that were artificially applied to the structure between inspection intervals. The results indicate that the integrated process is capable of generating models that accurately render a variety of defect types with sub-millimeter accuracy. Recommendations for mission planning and imaging specifications are provided as well.

Keywords: Infrastructure Inspection; Computer Vision; Structure from Motion; Dam Inspection; 3D Scene Reconstruction; Aerial Robots; Remote Sensing; Structural Health Monitoring; Unmanned Aerial Vehicles

1. Introduction

Dams are critical infrastructure systems for many communities, but they are also one of the most challenging to inspect due to their complex nature. Dams can experience a range of problems during their service life, and improper operation and maintenance result in major issues. Furthermore, dams can be deteriorated due to weathering, alkali-aggregate reaction (AAR, or alkali-silica reaction, ASR), freezing and thawing, or other chemical reactions. The Federal Emergency Management Agency (FEMA) publishes the Guidelines for Dam Safety [1], and suggest that formal inspections occur at least every 5 years. They also recommend informal, intermediate and special inspections as needed. The Maryland Department of Environment also recommends that owners inspect their dams after extreme rainfall and formally once every 5 years [2]. According to the American Society of Civil Engineers' (ASCE) 2017 Infrastructure Report Card [3] the average age of the 90,580 dams in the United States is 56 years, with 17% rated as high-hazard potential dams necessitating additional inspections.

The conventional standard of practice requires a detailed visual inspection not just of the primary structure, but of the subsystems and the surrounding watershed as well. Dams are typically very large and complex structures, and consequently dam inspections are time-intensive and require

© 2018 by the author(s). Distributed under a Creative Commons CC BY license.

Preprints (www.preprints.org) | NOT PEER-REVIEWED | Posted: 25 January 2018 doi:10.20944/preprints201801.0235.v1

expensive, specialized equipment and training to provide inspectors with comprehensive access to the structure. The scale and nature of dam inspections also introduces additional safety risks to the inspectors. Typically, a limited number of photographs, and occasionally videos, are captured to provide a visual record of the current state of the structure. By themselves, these recordings are not ideal data products, as reviewing them can be tedious and the lack of spatial context can prove disorienting to data analysts and engineers.

Recently, there have been advancements in the use of 3D imaging systems for capturing the *in-situ* 3D state of civil infrastructure systems [4]. The most widely used technology for generating 3D models, or point clouds, is Terrestrial Laser Scanning (TLS). A lower-cost alternative and somewhat complimentary approach is to use photogrammetric methods to extract 3D geometries from large sets of two-dimensional (2D) digital images. In either case, the result is a scale-accurate, high-resolution virtual model of a structure and its surrounding areas. These digital models capture current conditions of the entire structure that can be used for archival and analytical purposes [4, 5]. However, both 3D imaging approaches suffer from the same access challenges that hinder conventional visual inspections.

Unmanned aerial vehicles (UAV) are a disruptive innovation [6] with potential to transform traditional dam inspection methodologies by expanding the capabilities of 3D imaging in these environments. While UAV have been in use for some time, their recent popularity is in part due to reductions in hardware costs, improvements to software interfaces, and to the expanded range of sensor payload options [7]. The portability, mobility, and low cost of UAV can mitigate the need for expensive inspection access equipment and reduce safety risks to inspectors [8]. Furthermore, UAV serve as an almost ideal data collection platform for modern 3D reconstruction techniques. Critically, the nature of both UAV and 3D reconstruction methods necessitate careful planning and coordination to properly integrate and tailor these technologies for dam inspection.

1.1. Prior Work on Modern Dam Inspection

The reduced accessibility of dams, both for uptake needs and for their strategic nature, and the large amount of time needed for an inspection by traditional methods do not facilitate direct visual inspection. Therefore, novel methods that integrate modern remote sensing tools, robotics and computer vision techniques have been investigated in the past few years. In the work by Ridao et al. [9], an Autonomous Underwater Vehicle (AUV) was designed to collect images from a hydroelectric dam which was later used to generate photomosaic (with approximate resolution of 1 pixel/mm) of the inspected area to help with the visual inspection. González-Aguilera et al. [10] studied the viability of utilizing TLS systems to generate 3D models of a large concrete dam and further assessed its capability for structural monitoring. However, due to the limited access for data acquisition, the final model lacked the necessary completeness to capture the entire dam. Berberan et al. [11] studied using TLS for deformation monitoring of the downstream face of the Cabril Dam in Portugal using 3D models generated at two different times for comparison purposes. Although both of the aforementioned studies proved the value of 3D modeling using TLS for dam inspection, they were not able to capture the overall geometry and resolve the fine-scale (1mm) details needed for accurate visual inspection.

In the study by González-Jorge et al. [12], photogrammetric 3D modeling using UAV acquired imagery was tested for the monitoring of dam breakwaters. Recently, researchers have focused on using camera-equipped UAV to facilitate dam visual inspection through 3D modeling [13, 14]. Although using UAV provided unprecedented access to different parts of the dam at a lower cost, the complex geometry and large size of these structures made it impossible to reconstruct a complete model of the targeted structures.

In the recent work by Buffi et al. [15], UAV-based photogrammetry was used as a new tool for surveyors to generate a complete 3D model of the Rideacoli Dam in Italy. The generated model was compared against conventional techniques such as total stations, TLS and Global Positioning System (GPS) to assess the overall geometry captured through 3D photogrammetric approach. The evaluation results showed an accuracy within 2 centimeters, but the surface resolution (point density)

Preprints (www.preprints.org) | NOT PEER-REVIEWED | Posted: 25 January 2018 doi:10.20944/preprints201801.0235.v1

of the model was estimated to be an average of one point every 1 cm^2 which may be inadequate for detailed visual inspection of smaller scale damages such as cracks.

1.2. Contributions of This Work

This paper presents a case study on integrating aerial robots and 3D computer vision for visual inspection of a large gravity dam in the United States. A combination of multiple UAV platforms and photogrammetric approaches was used to create two comprehensive 3D point clouds of a dam and surrounding environment that were then assessed for their relative quality and ability to render artificially applied defects. The Brighton Dam, located in Brookeville, Maryland and managed by the Washington Suburban Sanitary Commission (WSSC), was selected as the subject of this study (Figure 1). The dam was put into service in 1944, and is representative of a large-scale gravity dam in-service across the United States.

Figure 1. The Brighton Dam.

The key technical contributions of this work include the development and assessment of a multi-UAV system for generating massive, dense, and comprehensive 3D point clouds (contain more than one billion points) of the targeted dam system, as well as an evaluation of the imaging specifications necessary to render small-scale inspection details. It is also the first time, to the authors' best knowledge, that a multi-scale photogrammetric 3D reconstruction technique has been used to capture the overall geometry of a large-scale complex gravity dam while simultaneously resolving structural flaws on the order of 1 mm using UAV-acquired images.

The details of the data collection procedure are presented first, followed by reporting of the operations on two inspection mission days. This is followed by a presentation of the data processing and analysis methodologies. An evaluation of the results of the methodological approach for the Brighton Dam inspection is included as well. The paper concludes with a summation of the findings of the research team and avenues for future work in this domain.

2. Data Collection

2.1. Logistics and Planning

The goal of the field testing was to collect two comprehensive sets of digital images to be converted into 3D point clouds, using a combination of DSfM and rigid registration techniques. The point clouds needed to have the point density—analogous to resolution—necessary to resolve inspection details on the millimeter scale while comprehensively capturing the overall spatial context of the dam. To achieve this, image acquisition in terms of camera positioning, the number of captured images, adjacent image overlapping, and image quality were all carefully considered.

Preprints (www.preprints.org) | NOT PEER-REVIEWED | Posted: 25 January 2018 doi:10.20944/preprints201801.0235.v1

A variant of the DSfM process previously developed by the research team was chosen to generate 3D point clouds [8, 16]. This process, referred to as Hierarchical Point Cloud Generation (HPCG), is designed to integrate images captured at a wide range of standoff distances from a structure into one complete model. From a data collection standpoint, images are collected in *networks* of similar standoff distances. The images from each network are then integrated and merged into a global, multi-scale point cloud model, as presented in the later sections of the paper.

Both fixed-wing and multi-rotor UAV platforms with mounted cameras were used to acquire image networks. The concept was to use the fixed wing UAV to capture the global geometry of both the upstream and downstream faces of the dam, and for the multi-rotor UAV to generate a series of oblique image networks from varying standoff distances. UAV flight planning that resulted in images with greater than 80% overlap between adjacent photos was desired to minimize the ground sample distance (GSD) and consequently maximize the spatial resolution. The minimum standoff distance from the dam was held to approximately 2.5m. This corresponded to a pixel size of approximately 0.0024 (mm/pixel) and a GSD of 0.6 mm in the plane of the dam façade for the lowest resolution sensor used during the project.

These images networks were collected over the course of two distinct days, in order to simulate variances in field conditions between inspection intervals and provide a basis for temporal analysis between the subsequent models. Data collection on the first day was designed to comprehensively image the entire dam and environs using a combination of three different UAV. Data collection on the second day focused on an isolated section of the dam that was selected for the defect analysis portion of the study, as will be discussed later.

A custom-built fixed wing mounted with a Sony Alpha Series 5100 camera (24.3-megapixels) with a Sony E-PZ 16–50 mm lens was used to capture a series of nadir angle shots that covered the dam and the surrounding area. The utilized UAV's airframe was the Super Sky Surfer fixed wing expanded polyolefin (EPO) foam frame. It was modified in order to custom fit various components, such as the autopilot, GPS module, airspeed sensor, camera payload, motor and batteries. The communication between the UAV and ground control station (GCS) was done through radio telemetry.

Two DJI Inspire 1 aircrafts mounted with 12-megapixel (MP) cameras were used to separately capture oblique imagery of the downstream and upstream portions of the dam. On the second day of data collection, in addition to capturing the entire dam structure, the mission was to focus on a specific region of the dam, Bay #5 of the downstream façade with preinstalled targets, which required maneuvering a UAV in a confined space. For this task, a DJI Phantom 4 Pro with a 16-MP camera, a smaller quadcopter aircraft, was selected due to its better maneuverability and collision avoidance features relative to the other available aircraft.

The logistics of flying multiple UAV over the two mission days, along with the complexities of the dam environment, meant that proper planning was essential. After the UAV pilots confirmed the test site was not in a restricted airspace, and that safe operations were feasible, the team began to target dates for data collection.

The performance of UAV inspection imaging is primarily dependent on operating conditions that do not impede piloting of the UAV itself. In particular, cold weather was a key consideration when identifying mission dates. The team determined that the battery life of the selected UAV would not operate sufficiently in temperatures below 5 degrees Celsius. Rain, snow, and high winds were also weather phenomena that dictated the ability to operate the UAV safely. Secondary to selecting mission days with viable UAV operating conditions, radiometric conditions that optimized the consistency of UAV imagery were preferred. High contrast lighting, typically due to bright sun conditions, can create strong shadows that degrade the performance of the DSfM process [8, 17].

2.2. Day One Operation

Mission planner software was used to develop a flight plan for the fixed wing nadir imaging that would allow the aircraft and camera to operate autonomously. A lawnmower pattern for an area of 174,502 m2 (Figure 2) was selected, at an elevation of 75 m. A camera intervalometer frequency of

Preprints (www.preprints.org) | NOT PEER-REVIEWED | Posted: 25 January 2018 doi:10.20944/preprints201801.0235.v1

1.69 seconds/image was specified, resulting in 558 nadir images (Figure 3). Total flight time for the fixed wing UAV was 26 minutes.

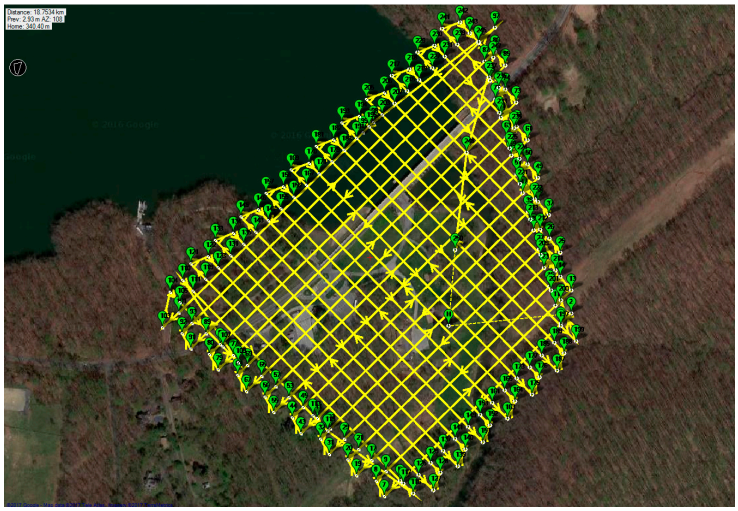

Figure 2. Flight path for fixed wing UAV.

The two rotary UAV were piloted manually, with a second operator controlling the camera and gimbal in order to guarantee the specified 80% overlap between images and maintain standoff distances, specified to maximize the quality of the DSfM reconstructions. In total 2020 images of the structure were captured using all three aircrafts.

Figure 3. Orthomosaic generated using the fixed wing imagery dataset.

2.3. Day Two Operation

The second day of operations also focused on Bay #5, on the downstream face of the dam. The goals of this day's operations were to generate a point cloud for comparisons with the point cloud generated through Day One operations, as well as to assess the quality of the UAV point cloud generation process for resolving small-scale structural defects.

Prior to UAV flight and imaging inside Bay #5, a series of controlled and simulated defects with known dimensions were applied to the dam structure, serving as a benchmark for reconstruction accuracy and analytical testing. Overall, three different types of defects were applied: linear markings with controlled thickness (Type 1), square surface area markings (Type 2), and spherical volumes (Type 3).

Preprints (www.preprints.org) | NOT PEER-REVIEWED | Posted: 25 January 2018 doi:10.20944/preprints201801.0235.v1

Type 1 defects were designed to simulate cracking and crack-like defects. Line thicknesses of 0.7mm, 1mm, and 3mm widths were applied, with lines varying in length from 12.7 mm to 152.4 mm for each width. The sets of lines were applied using both black and white chalk on the sides of Bay #5 (Figure 4). Type 2 defects were designed to simulate localized area defects such as concrete efflorescence, or staining due to corrosion. These defects took the form of a series of square chalk markings (Figure 4) with dimensions varying from 645 mm^2 to 16129 mm^2. Type 3 defects simulated volumetric changes, such as concrete spall off. As physically removing portions of the dam structure was not permissible, volumes were instead temporarily added to the structure. Three Styrofoam hemispheres, with diameters of 127 mm, 203.2 mm and 304.8 mm (Figure 4) were painted and textured to have the visual appearance of concrete, and placed on the lateral brace of Bay #5.

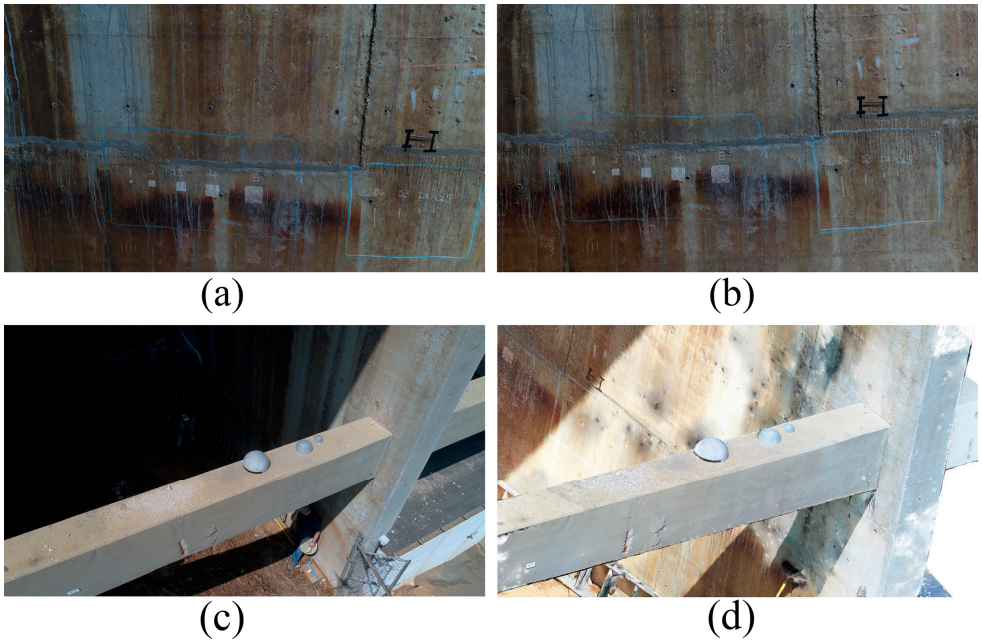

Figure 4. Controlled simulated damages: (**a**) 2D image of Type 1 and 2 defects; (**b**) 3D point cloud rendering of Type 1 and 2 defects; (**c**) 2D image of Type 3 volumetric defects; (**d**) 3D point cloud rendering of Type 3 volumetric defects.

2.4. Laser Scanning

For comparative purposes, a phase-shift based Faro Focus^{3D} laser scanner was used to collect data from downstream face of the dam. The quality of the data collection was set to 6x in order to reduce the noise in the scan data and thus increases the scan quality. Due to placement limitations, it was not possible to capture the upstream face of the dam with the scanner. A total of 9 scans was collected and merged using the Faro SCENE software.

3. 3D Point Cloud Generation

From the available algorithms for image-based 3D reconstruction techniques, in this work a variant of the *Structure-from-Motion* (*SfM*) process was chosen. SfM is based on the simultaneous recovery of both the 3D geometry (structure) of a scene and the camera pose (motion) using a sparse set of correspondences between image features, and has been shown to produce results comparable to laser scanners [17, 19].

The first step in the SfM process is to automatically detect keypoint feature descriptors (pixel locations that are highly distinctive) such as the Scale Invariant Feature Transform (SIFT) [20] in each input image. Next, feature descriptors are matched between pairs of images by finding a correspondence in the second image using a nearest neighbor similarity search [21] to construct the relationship of feature points between image pairs, called *tracks*.

Preprints (www.preprints.org) | NOT PEER-REVIEWED | Posted: 25 January 2018 doi:10.20944/preprints201801.0235.v1

Because corresponding points in two images are subject to the *epipolar constraints* (describe by the fundamental matrix), filtering the matches by enforcing these constraints removes false correspondences [18]. By using the normalized eight-point algorithm [22] in tandem with the RANSAC (RANdom SAmple Consensus) [23] paradigm, it is possible to minimize the number of wrong matches across images.

Next, an initial image pair with a large number of matched features and a long separation distance is selected and their camera parameters are estimated using the 5-point algorithm [24], followed by triangulation of the matched features using the polynomial method [25]. Subsequently, new images are added by using the correspondences between 3D points and image features through the *Perspective* n-*Point* (PnP) algorithm with RANSAC and Gauss-Newton optimization [26].

After the orientation of each image, bundle adjustment (a nonlinear least-squares problem) is performed to minimize the sum of *re-projection errors* using the Levenberg-Marquardt algorithm [27]. In this process intrinsic camera parameters matrix, *K*, along with the pose of each particular camera described by rotation, *R*, and the position of its optical center, *C*, as well as the positions of the 3D points *X* are optimized simultaneously.

$$\sum_{j}\sum_{i\in j}\left\|x_{ij}-\left(K_jR_j(X_i-C_j)\right)\right\|^2\rightarrow\min_{K_j,R_j,C_j,x_i} \tag{1}$$

Where $i\in j$ indicates that the point X_i is visible in image *j*, and x_{ij} denotes the projection of 3D points X_i onto image *j*. This procedure is repeated until an orientation is available for all images within each imaging network. The result of this pipeline is a relatively sparse set of 3D points, due to only utilizing extracted feature points in the 3D reconstruction.

In order to densify the reconstructed models and produce a model dense enough to capture small geometric changes, multi-view stereo algorithms [17] are used to capture information from all pixels in the input 2D images. In this work, the Semi-Global Matching (SGM) algorithm [28] was used to perform pairwise dense matching, as it has been shown to provide a high level of point density relative to other methods utilized for densification [16, 17]. The SGM algorithm uses a pixel-wise matching cost for compensating radiometric differences of registered images within the depth map estimation. Later, individual depth maps are merged together through *depth map fusion* technique to generate a single, globally consistent 3D representation [29].

The HPCG approach used in this study is designed for seamlessly matching and integrating images with different scales, viewpoints, and cameras into one single reconstruction [16]. The HPCG process begins by first generating 3D point clouds separately for each image network, using the aforementioned photogrammetric process. The point clouds generated for each network are then merged together into a single model using the Iterative Closest Point (ICP) algorithm [30]. The ICP approach refines the alignment assuming an initial coarse registration of the 3D models is provided. This initial alignment can be performed through pair-wise matching of 10 manually selected point correspondences in order to reduce the inherent sensitivity of the ICP algorithm regarding the initial positions of the 3D models.

The rigid transformation between two sets of *corresponding* 3D point sets $X=\{x_1,x_2,\cdots,x_N\}$ and $Y=\{y_1,y_2,\ldots,y_N\}$ extracted through utilizing *kd*-trees [21], can be formulated as the solution of the least-squares problem:

$$(R,t)=\underset{R,t}{\operatorname{argmin}}\sum_{n=1}^{N}\|(Rx_n+t)-y_n\|^2 \tag{2}$$

Where rotation matrix *R* and translation vector *t* can be derived by arranging the point in two 3×*N* matrices $\bar{X}$ and $\bar{Y}$ that have $\bar{x}_n$ and $\bar{y}_n$ as columns:

$$\bar{x}_n=x_n-\tfrac{1}{N}\textstyle\sum_{n=1}^{N}x_n\ ,\quad \bar{y}_n=y_n-\tfrac{1}{N}\textstyle\sum_{n=1}^{N}y_n \tag{3}$$

By computing the Singular Value Decomposition (SVD) of the 3×3 covariance matrix $\bar{X}\bar{Y}^T$, $U\sum V^T=SVD(\bar{X}\bar{Y}^T)$, the optimal *R* and *t* are given by:

Preprints (www.preprints.org) | NOT PEER-REVIEWED | Posted: 25 January 2018 doi:10.20944/preprints201801.0235.v1

$$R = V\begin{pmatrix} 1 & & \\ & 1 & \\ & & \det(VU^T) \end{pmatrix}U^T \ , \quad t = \frac{1}{N}\sum_{n=1}^{N} y_n - R\frac{1}{N}\sum_{n=1}^{N} x_n \tag{4}$$

These rotations and translations are then used to align the individual point clouds for each network and form the complete global model. The result is a multi-scale/resolution 3D model that allows for higher resolution and emphasis in critical regions of structures. This approach also increases the rate of image registration during the SfM process, thereby improving model accuracy, resolution and completeness.

3.1. Brighton Dam Model Generation

For this process to work properly there must be a global point cloud that captures the overall geometry of the structure, and into which the other point clouds are merged through ICP. In this work, this geometry network was captured using the fixed wing UAV. The second key criterion is that the standoff distances between merged point clouds cannot vary excessively. This was accomplished by capturing images at varying standoff distances (range from 2.5 m to 10 m).

4. Case Study Results

The images collected on Day One and processed using the HPCG technique yielded a point cloud of 1,469,690,005 points (Figure 5). The Day Two mission resulted in a model with 997,799,119 points.

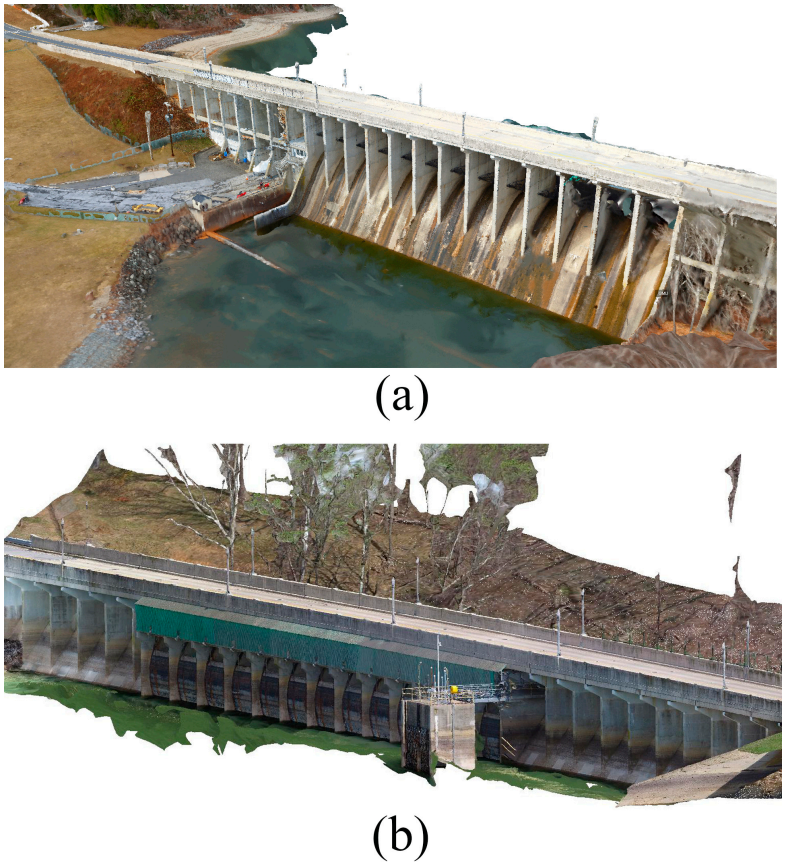

Figure 5. Generated 3D Point cloud of the Brighton Dam: (**a**) Downstream face; (**b**) Upstream face.

4.1. Point Cloud Quality Analysis

Three metrics were used to assess the point clouds: (i) local noise level, (ii) local point density, (iii) ability to resolve the controlled synthetic defects applied on mission Day Two.

Preprints (www.preprints.org) | NOT PEER-REVIEWED | Posted: 25 January 2018 doi:10.20944/preprints201801.0235.v1

The noise level in a point cloud is defined as the residual between each point and the best fitting plane computed on its local nearest neighbours. Digital image noise, radiometric parameters, nonconformity of the neighbourhood of a point, imperfect data registration, and DSfM reconstruction inaccuracies can all affect this characteristic.

This noise residual is defined as the lowest valued eigenvalue of the covariance matrix for a local neighborhood around a point in a cloud. For the k points that form the neighborhood of a 3D point p_i in a point cloud, the 3×3 covariance matrix, C, is defined as [31]:

$$C = \frac{1}{k}\sum_{i=1}^{k}(p_i - \bar{p})(p_i - \bar{p})^T; \quad \bar{p} = \frac{1}{k}\sum_{i=1}^{k} p_i \tag{5}$$

Where $\bar{p}$ is the arithmetic mean within p_i's neighbourhood (N_{pi}) and C represents a symmetric positive-definite matrix. By performing SVD on the covariance matrix, it is possible to compute eigenvectors V (v_2, v_1, and v_0) and their corresponding eigenvalues $\lambda_2 \geq \lambda_1 \geq \lambda_0 \geq 0$. Within this approach, v_0 approximates the point's p_i normal, while λ_0 quantitatively describes the variation along the normal vector to provide an estimation of the local noise level (i.e. roughness). In addition, the normalized surface variation or curvature (σ) can be defined as $\frac{\lambda_0}{\lambda_2+\lambda_1+\lambda_0}$, which is invariant under rescaling [32]. For this study a value of k=30 points was empirically specified for roughness calculations (Figure 6).

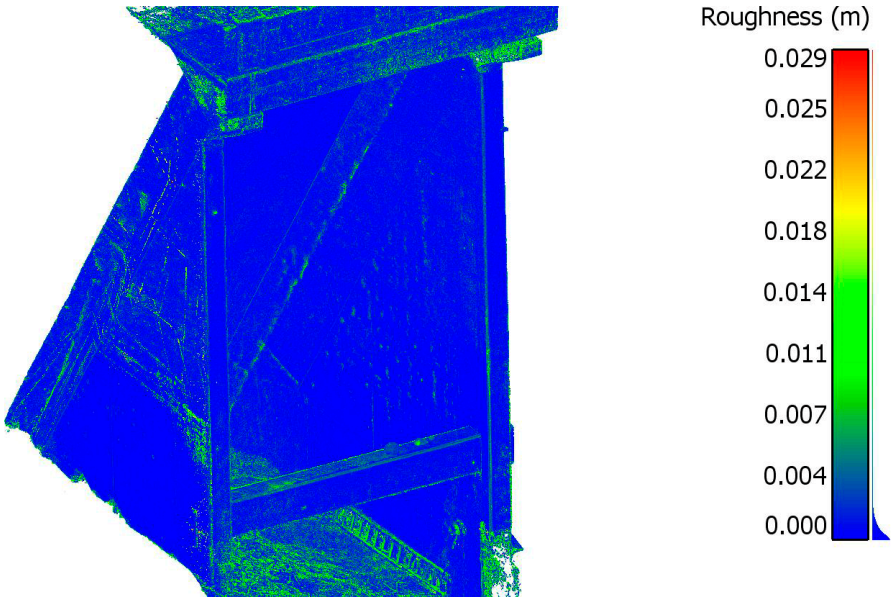

Figure 6. Estimated noise level (lowest eigenvalue λ_0) for Bay#5; low to high noise level ranges from dark to light intensity.

The second metric, local point density, is a characteristic analogous to pixel resolution in 2D digital images. It corresponds to the ability of a 3D point cloud to resolve structural defects and small-scale details. It also provides insight in the variations in point cloud quality that stem from the multi-UAV imaging approach. The local density ρ at a point p_i is defined as $\rho = \frac{k+1}{\frac{4}{3}\pi r_{k-NN}{}^3}$, where $r_{k\text{-}NN}$ is the radius of the spherical neighbourhood of the k closest neighbours of a 3D point. In this study, $r_{k\text{-}NN}$ was set to 0.62 centimeters to achieve an enclosing volume of 1 cm^3.

The last evaluative metric was to measure the defects applied to Bay #5 during the second mission day, in the resulting 3D point cloud. Both Type 1 and 2 simulated damages were manually measured from the point cloud models and the results was compared against the field measurements. In order to lessen the error, each manual pairwise point selection and its subsequent Euclidean distance measurement was repeated 10 times and their average value was compared against the ground-truth values measured in the field.

Volumetric defects (Type 3) were measured by using the direct cloud-to-cloud (C2C) distance estimation technique [33] to track and quantify geometrical changes in the already registered 3D

Preprints (www.preprints.org) | NOT PEER-REVIEWED | Posted: 25 January 2018 doi:10.20944/preprints201801.0235.v1

point clouds. Upon finding the closest point correspondences in the two registered clouds, the Hausdorff distance was utilized to find the distance between points in the first dataset and their closest points in the second dataset. Given two finite point sets $P = \{p_1, p_2, \cdots, p_n\}$ and $Q = \{q_1, q_2, \ldots, q_m\}$, the two-sided Hausdorff distance $H(P, Q)$ is defined as:

$$H(P,Q) = \max(\max_{p\in P} \min_{q\in Q} \|p-q\|, \max_{q\in Q} \min_{p\in P} \|q-p\|) \quad (6)$$

Note that this notation of distance is purely geometric and does not make any assumptions on the uniformity of the point cloud density. Using this method provided the radius of each hemisphere, which was later used to estimate their volume.

4.2. Point Cloud Analysis Results

The results of the point cloud quality analysis are shown in Table 1. Model density from the January UAV flights was substantially higher than those generated through TLS or during the April flights. The differences between the two HPCG models is likely due to the change in sensor resolution between mission days and changes in the flight protocols, as the April flights focused on Bay #5. Average roughness and curvature values for the three models are all of a similar order of magnitude, indicating relatively similar 3D geometric accuracy. As can be seen, the point cloud generated by the laser scanner consists of significantly fewer points than the models generated through HPCG. This was due to the limited options for scanner placement, particularly with respect to the higher elevation regions of the dam façade and the upstream façade. Point cloud quality analysis for the Bay #5 region of the dam are shown in Figure 7 and Table 2.

Table 1. Point Cloud Quality Analysis.

3D model	No. of points	Local Point Density (Points/cm³)	Mean roughness (mm)	Mean curvature
TLS (April 2017)	63,688,823	26.97	2.22	0.026
HPCG (January 2017)	1,469,690,005	53.94	1.47	0.029
HPCG (April 2017)	997,799,119	29.58	1.01	0.023

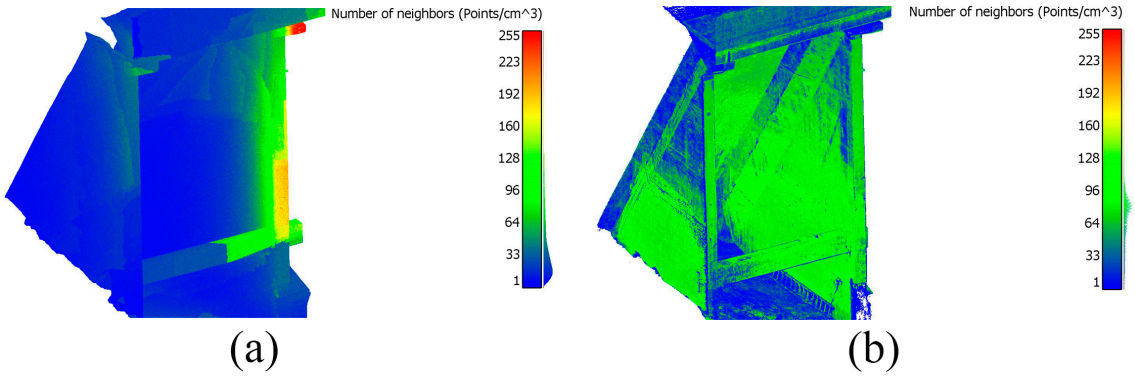

Figure 7. Local point density for Bay#5; low to high density ranges from dark to light intensity: (**a**) Day One dataset; (**b**) Day Two dataset.

These results highlight the advantages of using a UAV for point cloud generation. Both HPCG models had over twice the density and mean roughness values less than half those of the laser scanner. These performance improvements can be attributed to the ability of the UAV to capture high-resolution images at the higher elevations of the bay, whereas the laser scanner could only scan

Preprints (www.preprints.org) | NOT PEER-REVIEWED | Posted: 25 January 2018 doi:10.20944/preprints201801.0235.v1

354 those areas from the ground. Compared to the overall point cloud models, the results for the HPCG
355 models are more similar for Bay #5.

356 **Table 2.** Point Cloud Quality Analysis for Bay #5.

3D model	No. of points	Local Point Density (Points/cm³)	Mean roughness (mm)	Mean curvature
TLS (April 2017)	28,356,650	20.81	2.21	0.036
HPCG (January 2017)	108,286,272	56.19	0.92	0.026
HPCG (April 2017)	159,579,984	69.31	0.58	0.018

357 In order to assess how image resolution affected model quality, the images captured via UAV
358 during the April mission were downsampled to 50%, 25%, and 12.5% of the original image size using
359 the bicubic image interpolation. The downsampled images were then used to regenerate point clouds
360 of Bay #5. The resulting model assessments are shown in Table 3.

361 **Table 3.** Bay #5 3D Point Cloud Generation using Various Image Resolutions.

Image resolution (megapixels)	No. of points	Local Point Density (Points/cm³)	Mean roughness (mm)	Mean curvature
16 MP	159,579,984	69.31	0.58	0.018
8 MP	49,111,922	17.78	1.34	0.032
4 MP	12,820,420	4.71	2.41	0.047
2 MP	3,841,665	1.38	4.33	0.104

362 With a loss of image resolution, the density of the models is reduced, as expected. This reduction
363 does not scale linearly with the number of pixels, but quadratically. Notably, the average cloud
364 roughness increases with a reduction in image resolution, as can be seen in the images disparity maps
365 (Figure 8). This suggests that the reduced number of feature points used for SfM reconstruction along
366 with excessive noise within the depth map estimation and fusion (Figure 8) affected the accuracy and
367 quality of the resulting dense 3D point clouds.

Preprints (www.preprints.org) | NOT PEER-REVIEWED | Posted: 25 January 2018 doi:10.20944/preprints201801.0235.v1

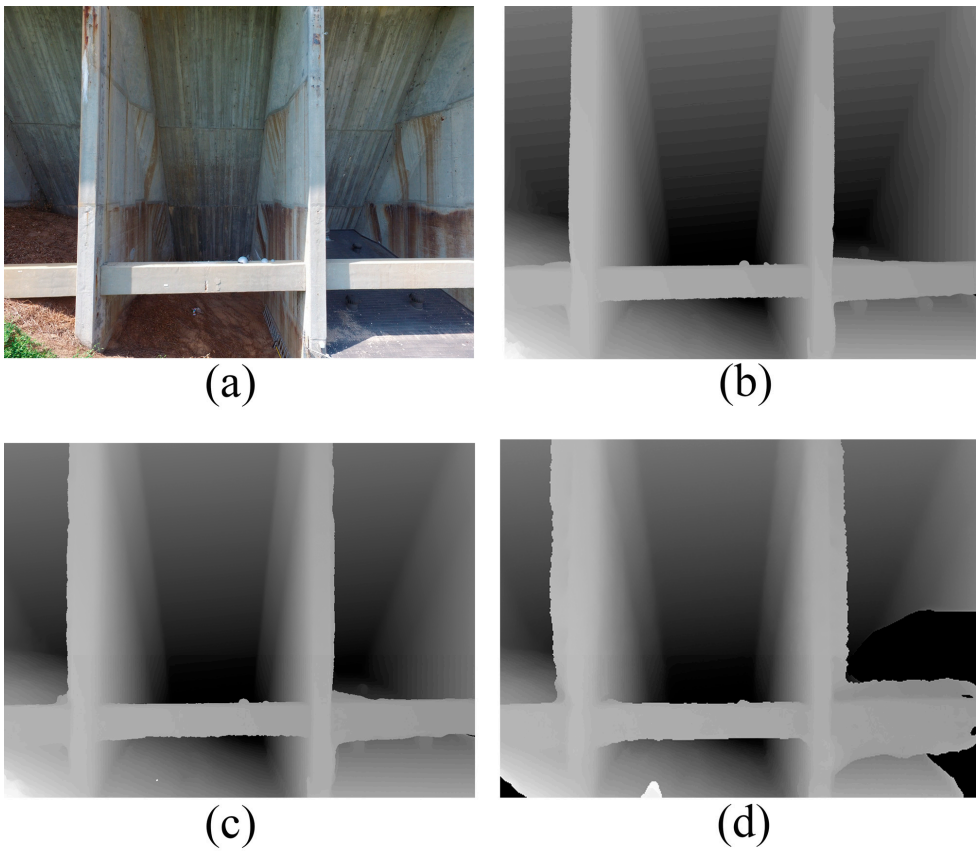

Figure 8. (**a**) Original input image; (**b**) depth map reconstructed for the 16 MP image; (**c**) depth map reconstructed for the 8 MP image; (**d**) depth map reconstructed for the 2 MP image. Each depth value encodes the distance from the camera center to the geometry.

4.3. Evaluation of Flaw Resolving Capabilities

Tables 4 and 5 summarize the comparisons between the ground-truth dimensions of the Type 1 defects and the dimensions measured in the point cloud. For the 1mm and 3mm defect widths, the point clouds generated using 16 MP images were able to resolve all of the flaws to a degree that highly accurate measurements were possible. However, as image resolution decreased, measurement accuracy decreased. For models using 4 MP or less in resolution, most flaws were not resolved at all in the models and so measurements were not possible. None of the models were able to reconstruct the 0.7mm flaws.

Table 4. Measurement Accuracy of 1 Millimeter Type 1 Defects at Various Image Resolutions.

Ground truth defect length	**Length measured in point cloud (mm)**			
(mm)	**16 MP**	**8 MP**	**4 MP**	**2 MP**
12.7	13	-	-	-
25.4	27.0	23	-	-
76.2	73	72	-	-
152.4	150.2	142	-	-

These results suggest that a point density somewhere between 18 points/m^3 and 69 points/m^3 was necessary to guarantee the reconstruction of Type 1 flaws in the model. During these tests, the standoff distance from the UAV to the defects was held at approximated 2.5 meters. Given the 16 MP

Preprints (www.preprints.org) | NOT PEER-REVIEWED | Posted: 25 January 2018 doi:10.20944/preprints201801.0235.v1

image resolution and the sensor dimensions of the DJI Phantom 4 camera, each pixel in the images corresponded to approximately 1mm in the plane of the defects.

Table 5. Measurement Accuracy of 3 Millimeter Type 1 Defects at Various Image Resolutions.

Ground truth defect length (mm)	Length measured in point cloud (mm)			
	16 MP	8 MP	4 MP	2 MP
12.7	13	10	-	-
25.4	26	25	-	-
76.2	76	72	68	-
152.4	151	152	139	-

The measurements for Type 2 defects are shown in Table 6. For these defects, the models derived from either the 16 MP (69 points/m^3) or the 8 MP (18 points/m^3) images were able to accurately resolve the flaws. However the 4 MP and 2 MP image models were not able to consistently resolve defects. This corresponds to a minimum pixel size of 1.5 mm in the plane of the defect.

Table 6. Measurement Accuracy of Type 2 Defects at Various Image Resolutions.

Ground truth defect size (mm × mm)	Size measured in point cloud (mm × mm)			
	16 MP	8 MP	4 MP	2 MP
25.4 × 25.4	26 × 25	26 × 24	-	-
50.8 × 50.8	51 × 50	52 × 51	-	-
76.2 × 76.2	76 × 76	76 × 76	62 × 70	-
101.6 × 101.6	100 × 100	97 × 100	98 × 93	-
127 × 127	127 × 127	125 × 125	121 × 125	-

The measurement results for the Type 3 volumetric defects are shown in Figure 9 and Table 7. For this test, all levels of image resolution were able to generate models that captured all three volumetric changes. However, the reduction in image resolution resulted in systematic under prediction of volume measurements.

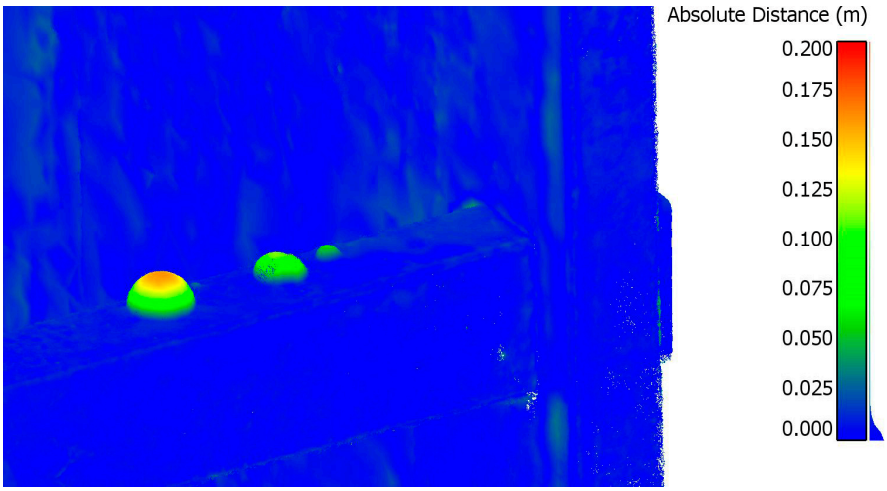

Figure 9. Volumetric 3D change analysis.

Preprints (www.preprints.org) | NOT PEER-REVIEWED | Posted: 25 January 2018 doi:10.20944/preprints201801.0235.v1

Table 7. Measurement Accuracy of Type 3 Volumetric Defects at Various Image Resolutions.

Ground truth defect size (mm^3)	Volume measured in point cloud (mm^3)			
	16 MP	**8 MP**	**4 MP**	**2 MP**
536265	430145	367809	190852	166519
2196540	2113300	2032190	1852990	1526810
7413330	7210900	7068580	6652890	6253830
Mean error	8.8%	14.5%	30.1%	38.4%

4.4. Limitations and Sources of Error

The process used to generate the point clouds has two key sources of error. The first is misalignment of cameras at the image matching stage. The second is misalignment of individual networks models during ICP registration. The quality and comprehensiveness of the point clouds was also impacted by the inability of the UAV to access certain regions of the structure. Specifically, certain interior regions and underwater sections of the dam were not imaged, and thus not included in the point cloud.

It is recognized that both of these areas would be critical for any inspection and assessment, and other methods of 3D imaging, such as handheld photogrammetry or laser scanning could be used in these circumstances. Furthermore, photogrammetric reconstruction techniques are sensitive to severe changes in lighting and occlusions. In this case study, UAV flight operations were restricted to minimize this effect, and further study on the impact of radiometric changes on model quality are warranted. Lastly, it is worth noting that the large number of points generated through this process (numbered in the billions) inhibits rendering and visualization. Out-of-core memory processes that decouple rendering efforts from the scale of the data in order to overcome memory limitations, are recommended to allow higher rendering frame rates and higher rendering quality during user interactions.

5. Conclusions

This study highlights the potential of using a combination of UAV and photogrammetry for the inspection and assessment of dam infrastructure. Ultimately, the goal was to generate models with sufficient density and quality to resolve a variety of critical inspection details at the millimeter scale. The mission protocols specified to achieve this were flight path planning that guaranteed sufficient image overlap at multiple standoff distances, as well as a minimum standoff distance that corresponded to a pixel size of 1mm, to guarantee reconstruction of defects at that scale. The assessment of the resulting models indicates that these specifications resulted in point clouds capable of rendering millimeter scale details, while lower density models generated with larger pixel sizes were often unable to resolve the artificial defects.

Future work seeks to study how to merge other sources of 3D point clouds, such as laser scanning and hand-held photogrammetry, with the model generated via UAV. Additionally, the process should be validated for a variety of infrastructure material types, and under varying radiometric conditions, to assess the reliability and consistency of the presented UAV inspection approach.

Acknowledgments: This material is based upon the work supported by the National Science Foundation (NSF) under Grant No. CMMI-1433765. Any opinions, findings, and conclusions, or recommendations expressed in this publication are those of the authors and do not necessarily reflect the views of the NSF.

Author Contributions: A.K., D.L., and A.J. conceived, designed, and performed the experiments; A.K. analyzed the data; A.K., D.L, and A.J. wrote the paper.

Conflicts of Interest: The authors declare no conflict of interest.

Preprints (www.preprints.org) | NOT PEER-REVIEWED | Posted: 25 January 2018 doi:10.20944/preprints201801.0235.v1

References

[1] U.S. Dept. Of Homeland Security, Federal Emergency Management Agency, *Federal Guidelines for Dam Safety*. Washington, DC: Federal Emergency Management Agency, 2004.

[2] Maryland Department of Environment, *Maryland Dam Safety Manual*. Baltimore, MD: Maryland Department of Environment, 1996.

[3] American Society of Civil Engineers, "2017 Infrastructure Report Card," American Society of Civil Engineers, Reston, VA, 2017.

[4] H. Fathi, F. Dai, and M. Lourakis, "Automated as-built 3D reconstruction of civil infrastructure using computer vision: Achievements, opportunities, and challenges," *Adv. Eng. Inform.*, vol. 29, no. 2, pp. 149–167, 2015.

[5] B. Jafari, A. Khaloo, and D. Lattanzi, "Deformation Tracking in 3D Point Clouds Via Statistical Sampling of Direct Cloud-to-Cloud Distances," *J. Nondestruct. Eval.*, vol. 36, no. 4, p. 65, Dec. 2017.

[6] C. Christensen, *The Innovator's Dilemma: When New Technologies Cause Great Firms to Fail*. Harvard Business Review Press, 1997.

[7] D. Turner, A. Lucieer, and C. Watson, "An Automated Technique for Generating Georectified Mosaics from Ultra-High Resolution Unmanned Aerial Vehicle (UAV) Imagery, Based on Structure from Motion (SfM) Point Clouds," *Remote Sens.*, vol. 4, no. 5, pp. 1392–1410, May 2012.

[8] A. Khaloo, D. Lattanzi, K. Cunningham, R. Dell'Andrea, and M. Riley, "Unmanned aerial vehicle inspection of the Placer River Trail Bridge through image-based 3D modelling," *Struct. Infrastruct. Eng.*, vol. 14, no. 1, pp. 124–136, Jan. 2018.

[9] P. Ridao, M. Carreras, D. Ribas, and R. Garcia, "Visual inspection of hydroelectric dams using an autonomous underwater vehicle," *J. Field Robot.*, vol. 27, no. 6, pp. 759–778, Nov. 2010.

[10] D. González-Aguilera, J. Gómez-Lahoz, and J. Sánchez, "A New Approach for Structural Monitoring of Large Dams with a Three-Dimensional Laser Scanner," *Sensors*, vol. 8, no. 9, pp. 5866–5883, Sep. 2008.

[11] A. Berberan, I. Ferreira, E. Portela, S. Oliveira, A. Oliveira, and B. Baptista, "Overview on terrestrial laser scanning as a tool for dam surveillance," in *6th International Dam Engineering Conference. LNEC, Lisboa*, 2011.

[12] H. González-Jorge, I. Puente, D. Roca, J. Martínez-Sánchez, B. Conde, and P. Arias, "UAV Photogrammetry Application to the Monitoring of Rubble Mound Breakwaters," *J. Perform. Constr. Facil.*, vol. 30, no. 1, p. 04014194, Feb. 2016.

[13] Elena Ridolfi, Giulia Buffi, Sara Venturi, and Piergiorgio Manciola, "Accuracy Analysis of a Dam Model from Drone Surveys," *Sensors*, vol. 17, no. 8, p. 1777, Aug. 2017.

[14] M. J. Henriques and D. Roque, "Unmanned aerial vehicles (UAV) as a support to visual inspections of concrete dams," presented at the Second International Dam World Conference, Lisbon, Portugal, 2015.

[15] G. Buffi, P. Manciola, S. Grassi, M. Barberini, and A. Gambi, "Survey of the Ridracoli Dam: UAV–based photogrammetry and traditional topographic techniques in the inspection of vertical structures," *Geomat. Nat. Hazards Risk*, pp. 1–18, Aug. 2017.

[16] A. Khaloo and D. Lattanzi, "Hierarchical Dense Structure-from-Motion Reconstructions for Infrastructure Condition Assessment," *J. Comput. Civ. Eng.*, p. 04016047, 2016.

[17] F. Remondino, M. G. Spera, E. Nocerino, F. Menna, and F. Nex, "State of the art in high density image matching," *Photogramm. Rec.*, vol. 29, no. 146, pp. 144–166, Jun. 2014.

[18] R. Hartley and A. Zisserman, *Multiple view geometry in computer vision*, Second. Cambridge, UK: Cambridge university press, 2004.

Preprints (www.preprints.org) | NOT PEER-REVIEWED | Posted: 25 January 2018 doi:10.20944/preprints201801.0235.v1

[19] S. M. Seitz, B. Curless, J. Diebel, D. Scharstein, and R. Szeliski, "A Comparison and Evaluation of Multi-View Stereo Reconstruction Algorithms," in *2006 IEEE Computer Society Conference on Computer Vision and Pattern Recognition*, 2006, vol. 1, pp. 519–528.

[20] D. G. Lowe, "Distinctive Image Features from Scale-Invariant Keypoints," *Int. J. Comput. Vis.*, vol. 60, no. 2, pp. 91–110, Nov. 2004.

[21] M. Muja and D. G. Lowe, "Scalable Nearest Neighbor Algorithms for High Dimensional Data," *IEEE Trans. Pattern Anal. Mach. Intell.*, vol. 36, no. 11, pp. 2227–2240, Nov. 2014.

[22] R. I. Hartley, "In defense of the eight-point algorithm," *IEEE Trans. Pattern Anal. Mach. Intell.*, vol. 19, no. 6, pp. 580–593, Jun. 1997.

[23] M. A. Fischler and R. C. Bolles, "Random Sample Consensus: A Paradigm for Model Fitting with Applications to Image Analysis and Automated Cartography," *Commun ACM*, vol. 24, no. 6, pp. 381–395, Jun. 1981.

[24] D. Nister, "An efficient solution to the five-point relative pose problem," *IEEE Trans. Pattern Anal. Mach. Intell.*, vol. 26, no. 6, pp. 756–770, Jun. 2004.

[25] R. I. Hartley and P. Sturm, "Triangulation," *Comput. Vis. Image Underst.*, vol. 68, no. 2, pp. 146–157, Nov. 1997.

[26] V. Lepetit, F. Moreno-Noguer, and P. Fua, "EPnP: An Accurate O(n) Solution to the PnP Problem," *Int. J. Comput. Vis.*, vol. 81, no. 2, pp. 155–166, Feb. 2009.

[27] C. Wu, S. Agarwal, B. Curless, and S. M. Seitz, "Multicore bundle adjustment," in *CVPR 2011*, 2011, pp. 3057–3064.

[28] H. Hirschmuller, "Stereo Processing by Semiglobal Matching and Mutual Information," *IEEE Trans. Pattern Anal. Mach. Intell.*, vol. 30, no. 2, pp. 328–341, Feb. 2008.

[29] S. Fuhrmann and M. Goesele, "Fusion of Depth Maps with Multiple Scales," in *Proceedings of the 2011 SIGGRAPH Asia Conference*, New York, NY, USA, 2011, p. 148:1–148:8.

[30] P. J. Besl and N. D. McKay, "Method for registration of 3-D shapes," presented at the Robotics-DL tentative, 1992, vol. 1611, pp. 586–606.

[31] K. Klasing, D. Althoff, D. Wollherr, and M. Buss, "Comparison of surface normal estimation methods for range sensing applications," in *IEEE International Conference on Robotics and Automation, 2009. ICRA '09*, 2009, pp. 3206–3211.

[32] M. Pauly, M. Gross, and L. P. Kobbelt, "Efficient Simplification of Point-sampled Surfaces," in *Proceedings of the Conference on Visualization '02*, Washington, DC, USA, 2002, pp. 163–170.

[33] D. Girardeau-Montaut, M. Roux, R. Marc, and G. Thibault, "Change detection on points cloud data acquired with a ground laser scanner," *Int. Arch. Photogramm. Remote Sens. Spat. Inf. Sci.*, vol. 36, no. part 3, p. W19, 2005.